Picometer-scale atom position analysis in annular bright-field STEM imaging

Peng Gao [a,b,c,*], Akihito Kumamoto [a], Ryo Ishikawa [a], Nathan Lugg [a,d], Naoya Shibata [a,d], Yuichi Ikuhara [a,d]

[a] Institute of Engineering Innovation, School of Engineering, University of Tokyo, Tokyo 113-8656, Japan
[b] Electron Microscopy Laboratory, and International Center for Quantum Materials, School of Physics, Peking University, Beijing 100871, China
[c] Collaborative Innovation Center of Quantum Matter, Beijing 100871, China
[d] Nanostructures Research Laboratory, Japan Fine Ceramic Center, Nagoya 456-8587, Japan

ARTICLE INFO

ABSTRACT

We study the effects of specimen mistilt on the picometer-scale measurement of local structure by combing experiment and simulation in annular bright-field scanning transmission electron microscopy (ABF-STEM). A relative distance measurement method is proposed to separate the tilt effects from the scan noise and sample drift induced image distortion. We find that under a typical experimental condition a small specimen tilt ($\sim$6 mrad) in 25 nm thick $SrTiO_3$ along [001] causes 11.9 pm artificial displacement between O and Sr/TiO columns in ABF image, which is more than 3 times of scan noise and sample drift induced image distortion $\sim$3.2 pm, suggesting the tilt effect could be dominant for the quantitative analysis of ABF images. The artifact depends on the crystal mistilt angle, specimen thickness, defocus, convergence angle and uncorrected aberration. Our study provides useful insights into detecting and correcting tilt effects during both experiment operation and data analysis to extract the real structure information and avoid mis-interpretations of atomic structure as well as the properties such as oxygen octahedral distortion/shift.

1. Introduction

Local structure distortion at grain boundary, hetero-interface, dislocation and surface can significantly influence on a broad variety of physical properties in complex oxide materials. Precise measurement of atom positions at these defects enables us quantitatively analyze the local strain field, electric dipole, flexoelectric effects, and chemical valence and thus provide new insights into understanding as to how materials properties depend on the local atomic structures and how we can engineer defects to optimize the materials or devices. Traditional crystallographic structure analysis such as x-ray or neutron diffraction is inadequate for the local structure analysis because of the poor spatial resolution. The recent advances in aberration corrected (scanning) transmission electron microscopy (S/TEM), however, can allow us to directly measure the inter-atomic distances with picometer-precision, providing a unique tool to study the local structure distortion. For examples, Bals et al. measured the local atomic structure of $Bi_4W_{2/3}Mn_{1/3}O_8Cl$ by using exit wave reconstruction [1]. Jia et al. directly mapped the electric dipoles in ferroelectric thin films by using negative C_s TEM observations [2]. The atomic displacements at ferroelectric domain walls in $BiFeO_3$ and $PbZr_{0.2}Ti_{0.8}O_3$ thin films are studied by measuring annular dark-field (ADF) STEM and TEM images from different groups [3,4]. Yankovich et al. reported sub-picometer precision measurement of Si lattice in ADF-STEM imaging [5]. In TEM mode, the exit wave reconstruction or negative C_s condition require systematic simulations for the interpretation of image contrast and also very thin specimens (typically less than 5 nm). For the atomic-resolution STEM imaging, the interpretation of image contrast is much straightforward and reliable [6–8], and it is also capable of simultaneous spectroscopy, being powerful to characterize the local structural and chemical properties. However, in the ADF-STEM images (Z-contrast, Z is atomic number), the functional light elements such as lithium or oxygen are usually invisible when the compounds contain relatively heavier elements. In contrast, the ABF imaging [8–12] are able to simultaneous visualize both heavy and light element atomic columns over a wide range of thickness (typically more than 50 nm), allowing us to determine the positions of full atomic species from a single image. Therefore, ABF-STEM imaging is one of best

* Corresponding author at: Electron Microscopy Laboratory, and International Center for Quantum Materials, School of Physics, Peking University, Beijing 100871, China.
E-mail addresses: p-gao@pku.edu.cn (P. Gao), ikuhara@sigma.t.u-tokyo.ac.jp (Y. Ikuhara).

candidate for the quantitative measurement of local structure distortion, especially for the complex oxides analysis [13–20].

Generally, the measurement precision of inter-atomic distance in STEM image is limited by scan noise and image distortion originated from the specimen drift (we use 'scan distortion' hereinafter). Several methods, therefore, have been employed to correct the scan distortion [5,21–24]. In fact, the specimen tilt is another important factor that could influence on the contrast and deformation of the atom-shape, as reported in ADF-STEM [25–33] due to the reduction in strength of the electron beam channeling [34]. On the basis of dynamical scattering theory, Van Dyck et al. discussed the effects of different range of specimen tilt [25]. Maccagnano-Zacher et al. pointed out that a specimen tilt reduces the contrast in atomic-resolution ADF-STEM [26]. So et al. reported that a specimen misalignment can cause a shift of atomic columns [27]. In the ABF image, the contrast of light atomic columns are basically related to forward elastic scattering, whereas the contrast of heavy atomic columns are contributed from both thermal diffuse scattering (TDS) and elastic scattering components [8]. Unlike the TDS signal (incoherent), the elastic scattering (coherent) contrast is very sensitive to the specimen conditions. One example is that the intensity of ABF image oscillates along the thickness, which becomes significant for the thin specimen and/or light atomic columns [8]. Therefore, the tilt effect in ABF image contrast is likely more sensitive than in ADF images, which has been firstly pointed out by Findlay et al. based on the SrTiO$_3$ (STO) simulations [8]. Recently, Gao et al. reported that the crystal tilt might cause significant artifact in interpretation of the ferroelectric polarization phenomena in ABF images [13,35]. Zhou et al. studied the deviation of atom positions between ABF and ADF and the effect of tilt on the bond angle measurements in ZrO$_2$ [36]. Liu et al. reported the effects of crystal tilt on the relative positions in PbTiO$_3$ in both ADF- and bright filed (BF) STEM images and found that tilt effect strongly depends on the tilt-angle and the specimen thickness [37]. Brown et al. proposed a new method to detect and correct the specimen tilt by simultaneously recording a central bright-field imaging (c-BF) and ABF images [38]. Recently, Kim et al. compared the BF and ABF and discussed the reliability of oxygen octahedral tilts measurements as function of specimen tilts and defocus [15].

In this paper, we combine experiments and simulations to quantitatively study the small specimen tilt effects on the atom position analysis of ABF images with an emphasis on calculating and correcting the artifact, and avoiding mis-interpretation of local atomic structure. Since the tilt is always mixed with scan distortion in experimental images, we introduce a new method, relative-distance measurement, to separate the tilt effects from other factors. We choose perovskite STO (ABO$_3$) single crystal with perfect cubic structure as a demonstration to discuss the tilt effects on quantitative measurement of atomic column positions in ABF-STEM imaging. In a perovskite structure, the rigid oxygen octahedron exhibits various structural distortions driven by stain and electrostatic conditions, underpinning many functionalities. Many efforts have been paid to precisely measure the local distortion in perovskite structures by various microscopy techniques [2–4,32,39–53] including ABF-STEM imaging [12–20,35]. In our work, we use a probe corrected ARM300CF (JEOL Ltd.) microscope, operating at 300 kV, and we simultaneously record both ADF- and ABF-STEM images, where a convergence semi-angle is 24 mrad, detector collection semi-angles spanning from 65 to 200 mrad for ADF and 12 to 24 mrad for ABF imaging, respectively. We also have performed systematic multi-slice image simulations for quantitative comparison with experiment. Dynamical image simulations in STEM were carried out by using commercial software of HREM Research, Inc. The Debye-Waller factors for Sr, Ti and O are given in the previous literature [54].

We find that, in the tilted crystal, the atom position shift strongly depends on atom species, leading to significant artifacts in distance measurement between the light anion columns and heavy cation columns, i.e., artificial atomic displacements. Under typical convergence semi-angle of 24 mrad, even with the small tilt of 6 mrad (0.34°) with 25 nm thick STO viewing along the [001] direction, the artificial displacement is estimated to be 11.9 pm between cation and anion atoms, which must lead to significant mis-interpretation of local atomic structure. This artificial displacement is much larger than that induced by scan distortion (a few picometers in distance). This artificial displacements depend on the tilt angle, defocus, thickness of the specimen, convergence angle and uncorrected aberration. Under some certain experimental conditions such as small size of aperture, such artifacts can be even more significant. For example, if 10 mrad convergence semi-anlge is chosen for the same specimen, the artificial displacement can be larger than 30 pm, even the tilt is as small as 0.5 mrad. In such cases, it is critical to consider the tilt effect for the precise measurement of atom positions in ABF images. We present in details on mechanism of formation, estimation and correction of the artifact, providing useful insights into local structure measurements of ABF images with specimen tilt.

2. Method

The electron transparent specimen of STO were prepared by mechanical polishing the single crystal followed by Ar ion milling (Precision Ion Polishing System, Gatan). Fig. 1(a) and (b) are simultaneously recorded ADF and ABF images along the [001] direction with sampling rate of ∼5 pm per pixel [55]. The images are averaged from multiple fast scanned frames after alignment to minimize the drift effect. Generally, the coexist of specimen tilt and drift effects are difficult to separate. However, in the case of sequential imaging, the effect of specimen drift (scan distortion) can be minimized and thus the tilt effects stand out. Atomistic structure model is overlaid on the images and highlights the positions of Sr, TiO and O columns in Fig. 1(a) and (b). Fig. 1(c) is the contrast inverted ABF image (*I*-ABF) in which the atom positions and the contrast-deformation of atoms are easier to distinguish. Fig. 1(d)–(f) show the unit-repeated-averaged images to reduce the scan distortion. Although the bulk of single crystal STO must have a perfect cubic structure without any oxygen octahedral distortion/shift, the O columns in Fig. 1(f) are not at the symmetric positions relative to cation columns, and instead shift to bottom-right direction due to the specimen tilt.

To elucidate such a subtle displacement, all the atom columns in both ADF and ABF images are fitted to two-dimensional (2D) Gaussian function using a home-developed MATLAB code [3,45–49,51] to minimize the effects of scan distortion. The 2D Gaussian peaks rather than the apexes are used to precisely determine the atom positions with sub-pixel precision (∼ 0.5 pm precision). Note that we used raw atomic-resolution STEM images without any post-filtering. Intensity profiles in Fig. 1(g)–(i) show that the fitted 2D Gaussian profiles reproduce the experimental intensity profiles.

For the evaluation of the specimen tilt, we here use the displacement vector of A-type column relative to the center of B-type sub-lattices. At this geometric configuration as illustrated in Fig. 2(a) and (b), we can reasonably ignore a small constant specimen drift because of subtraction process. In the case of drift-free, the displacement vector is $D = P_A - C_B$, where P_A is the fitted atom position of A-type column and C_B is the center position of B-type sub-lattices. The specimen drift velocity V is assumed to be constant under a short period of recording one-unit cell rows (∼160 ms). The pixel corresponding to A-type column position is recorded at the time t_A, and the pixels for four B-type
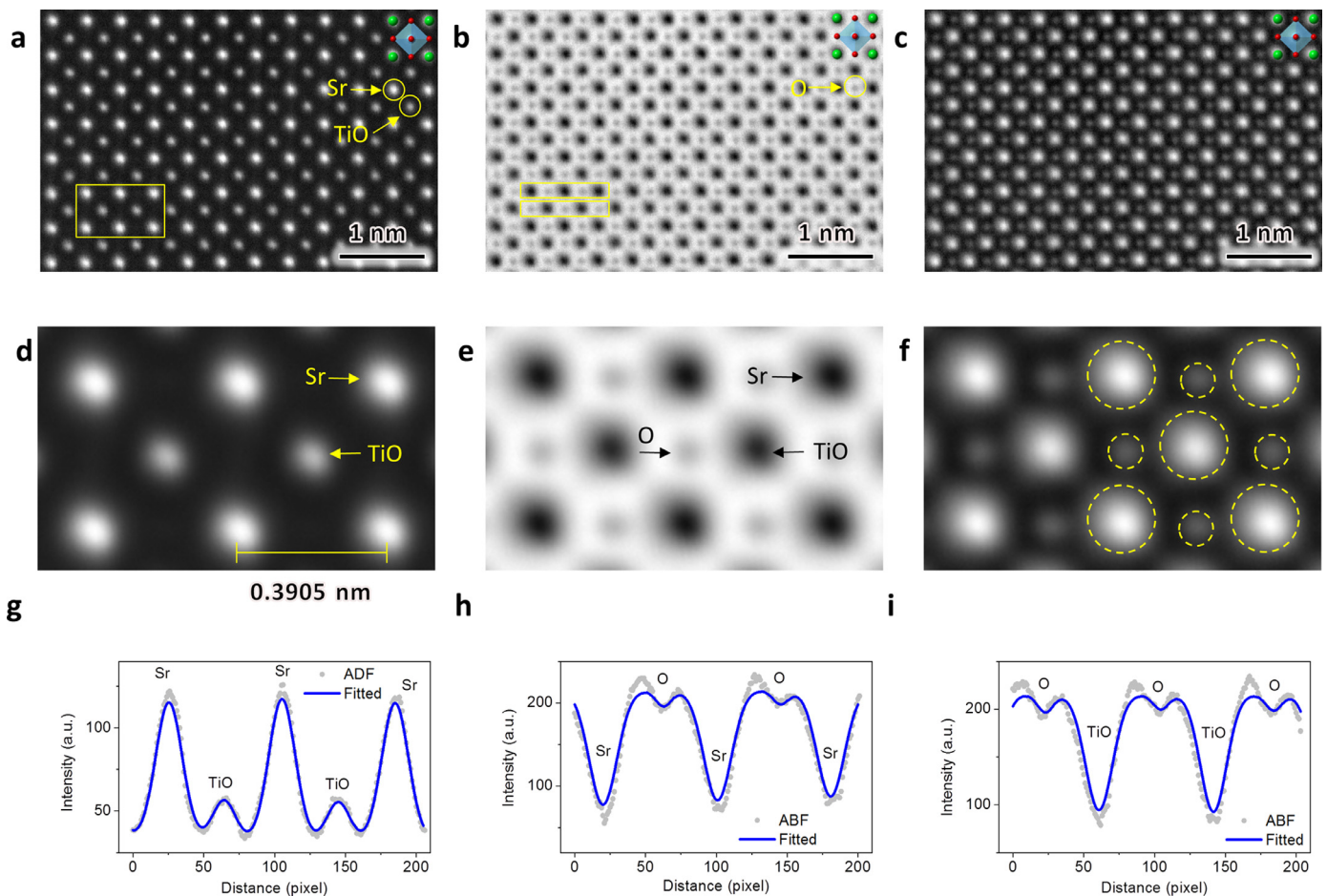
Fig. 1. (a) Raw ADF-STEM image from a single crystal SrTiO$_3$ (STO) with zone axis close to [0 0 1]. (b) Simultaneously recorded ABF and (c) contrast inverted ABF (*I*-ABF) images. Unit cell averaged (d) ADF, (e) ABF and (f) *I*-ABF images. The yellow circles in (f) roughly highlighting the position of atom columns. The O columns slightly shift toward right-bottom corner. Intensity profiles of raw experimental and Gaussian fitted (g) ADF and (h, i) ABF images from the regions highlighted in (a) and (b). (For interpretation of the references to color in this figure legend, the reader is referred to the web version of this article)

column positions are recorded at t_{B1}, t_{B2}, t_{B3}, and t_{B4}. Approximately $t_A = (t_{B1} + t_{B2} + t_{B3} + t_{B4})/4$ for the single crystal STO viewing along [100]. In the case of a small drift, the displacement vector becomes $D' = P_A' - C_B'$, where the position of A-type column is $P_A' = P_A + Vt_A$, and the center position of four B-type columns is $C_B' = C_B + V(t_{B1} + t_{B2} + t_{B3} + t_{B4})/4$ if the small drift is a constant. In this case, D' is equivalent to D, indicating such relative displacement vector is independent of the specimen drift. Therefore, the measured value from experimental STEM images should be mainly due to the specimen tilt. We consider the following displacement vectors with four types of sub-lattices is given in Fig. 2(c): Sr *vs* TiO (cation sub-lattice), TiO *vs* Sr (cation sub-lattice), O *vs* O (anion sub-lattice), and O *vs* Sr/TiO (mixture sub-lattice) columns. In each configuration of A *vs* B, the sign of vector is inverted for the *A*-type to maintain a constant direction in the vector mapping.

In practice, the specimen drift vector is not an exact constant even within a short dwell time, consisting of both 'low' and 'high' frequency components. Though the low frequency component can be negligible as a constant for the displacement vector, the high frequency component still exists in STEM images and leads to variable relative displacements in each unit cells. However, the high frequency component is noise-like and we will treat it as a scan noise hereinafter. Although the low frequency component causes a significant change in lattice including lattice aspect ratio and angle between lattice vectors in STEM images (e.g., A-A distance, B-B distance, A–A–A angle etc.), the specimen tilt does not because the

atom shift induced by the specimen tilt is exactly the same for the crystallographically same atom columns, and therefore the lattice aspect ratio and lattice vectors angle (A–A–A angle but not A–B–A angle) should be irrelevant with specimen tilt at all. In this regard, the specimen tilt effect and low frequency component of the specimen drift can be reasonably separated, while the effects of high frequency of the specimen drift can be minimized by the 2D Gaussian fitting atom positions and thus ignored for the distance measurements in our study.

3. Results

3.1. Experimental analysis

The experimental STEM images are analyzed in Fig. 3. Since the STO single crystal has an ideal cubic structure, any structure deviation from cubic in the images should be artifact caused by specimen tilt, scan distortion and/or aberration. Based on the discussion above, the atomic displacements are analyzed to evaluate the tilt effect in Fig. 3(a)–(f), while the lattice constant, lattice ratio, and bond angle are analyzed to evaluate the low frequency component of scan distortion in Fig. 3(g)–(i).

Fig. 3(a) and (b) show the displacement vector maps of cation sub-lattices (TiO column that is a Ti-O-Ti-O-Ti…chain along the electron beam direction is considered as a cation column hereinafter) in ADF and *I*-ABF images, respectively. Fig. 3(c) is the
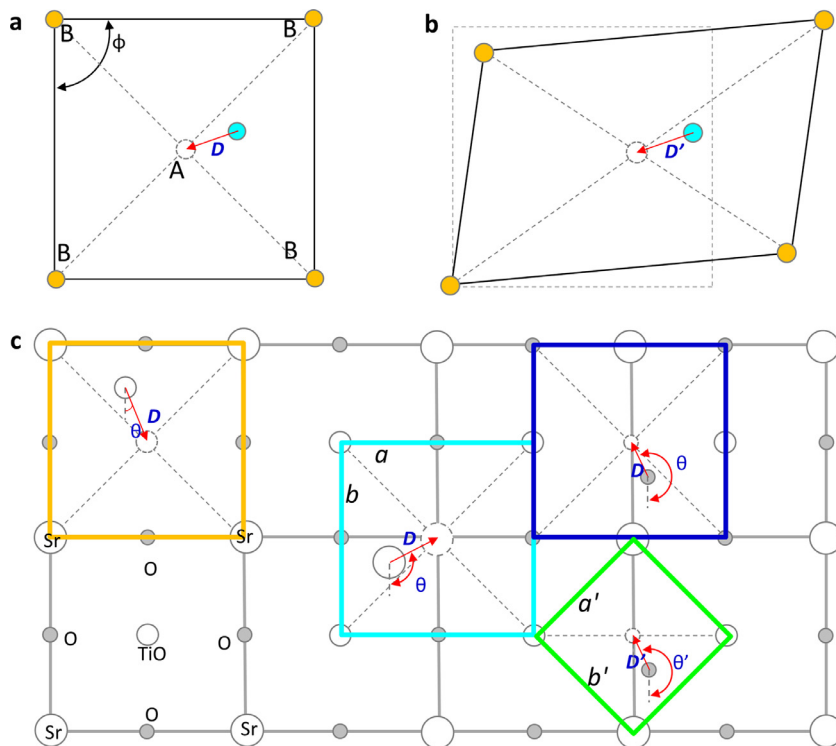
Fig. 2. Schematic showing relative distance measurement in STEM images to separate the tilt effect from the specimen drift. The STO is viewed along [001] direction. (a) No specimen drift. The displacement vector of A column relative to the center of four nearest B columns is ***D***. (b) With specimen drift, B column sub-lattice is not square anymore. The displacement vector of A column relative to the center of four nearest B column sub-lattice is ***D'***. (c) Schematic showing four types of sub-lattice configuration in STEM images. Orange: the displacement of TiO column relative to the center of nearest Sr columns. Cyan: the displacement of Sr column relative to the center of nearest TiO columns. Blue: the displacement of O column relative to the center of neighboring O columns. Green: the displacement of O column relative to the center of neighboring TiO and Sr columns. (For interpretation of the references to color in this figure legend, the reader is referred to the web version of this article)

vector map of anion sub-lattice in *I*-ABF image. However, for the mixture sub-lattice in *I*-ABF image in Fig. 3(d), the directionality is clearly recognizable, indicating the specimen tilt induced artifact is pronounced. The amplitude and orientation of the displacement vectors for these four sub-lattices are summarized in histograms in Fig. 3(e) and (f), respectively. In Fig. 3(e), the average amplitude of the displacement vectors in cation sub-lattices is (2.9 ± 1.5) pm (red) for ADF image and (4.0 ± 1.7) pm (yellow) for ABF image. The measured deviation in ADF image is slightly smaller than that of ABF image, because ADF image has higher signal-to-noise-ratio (SNR) than that of ABF. For anion sub-lattice in *I*-ABF image, the mean value is (7.0 ± 3.8) pm (green) and the standard error becomes larger than that in the case of cation sub-lattice. This lower precision is attributed to the lower SNR in contrast and fewer pixels for fitting O atom columns. For the mixture sub-lattice in *I*-ABF image, the amplitude (19.0 ± 3.5) pm of displacement vectors in Fig. 3(e) (blue) is much larger than those calculated from other sub-lattices (red, yellow, and green). Furthermore, the corresponding direction of the vectors is highly ordered as shown in Fig. 3(f) (blue), contrasting to approximately random orientation of other sub-lattices (red, yellow, and green). Such artifact leads to significant mis-interpretation of microstructure and properties in oxides such as ferroelectricity. It is noteworthy that 19 pm cation displacement relative to the anion in perovskite is the same order of the spontaneous polarization in perovskite ferroelectrics, i.e., 19 pm corresponds to $\sim$19 $\mu C/cm^2$ for displacement between Pb and O in $PbTiO_3$ and $\sim$ 32 $\mu C/cm^2$ for displacement between Ti and O based on the Born effective values from literature [56].

The low frequency component of the scan distortion mainly causes the change in lattice constant, lattice ratio and the angle between lattice vectors in STEM images. For each sub-lattice configurations, the lattice constant (e.g. Sr-Sr distance), bond angle (e.g. Sr–Sr–Sr angle), and lattice ratio are calculated in Fig. 3(g)–(i). In Fig. 3(g), the standard deviation of the measured lattice constant from the ABF image is 3.3 pm (0.83% of lattice constant) for cations sub-lattice (yellow), while for anions sub-lattice (green) this value, 6.0 pm, is slightly larger due to the lower SNR as discussed above. The lattice ratio a/b is 1.008 ± 0.012 (corresponding to 3.2 ± 4.8 pm in distance) in Fig. 3(h) and the bond angle is $(89.6 \pm 0.65)°$ (corresponding to 2.8 ± 4.4 pm in distance) in Fig. 3(i) for cations sub-lattice (yellow), whereas the distribution of anion sub-lattice (green) is also slightly broader due to lower SNR. The relative large standard deviation of lattice ratio and angle suggests a non-uniform lower frequency scan distortion during recording the entire image. For the mixture sub-lattices of O *vs* Sr/TiO configuration (blue histograms in Fig. 3(g)–(i)), the measurements of lattice constant, bond angle, and lattice ratio have no obvious difference from the others except slightly broad distribution due to lower SNR, indicating the scan distortion induced artifacts in lattice constant, bond angle, and lattice ratio are similar for these four different sub-lattice configurations.

Overall, for the artifacts in the ABF image, the scan distortion induced artifact is on the level of $\sim$3.2 pm that is relatively small compared to the tilt induced displacement $\sim$19 pm, indicating it is critical to consider the tilt effect for the quantitative ABF analysis. Furthermore, such small scan distortion effect is profit from the use of sequential imaging [55].

3.2. Simulation

It is difficult to distinguish the effects of specimen mistilt from the optical misalignments in STEM. In order to elucidate quantitative information of the net specimen mistilt, a series of STEM images are simulated. Fig. 4(a) shows the tilt dependence of the
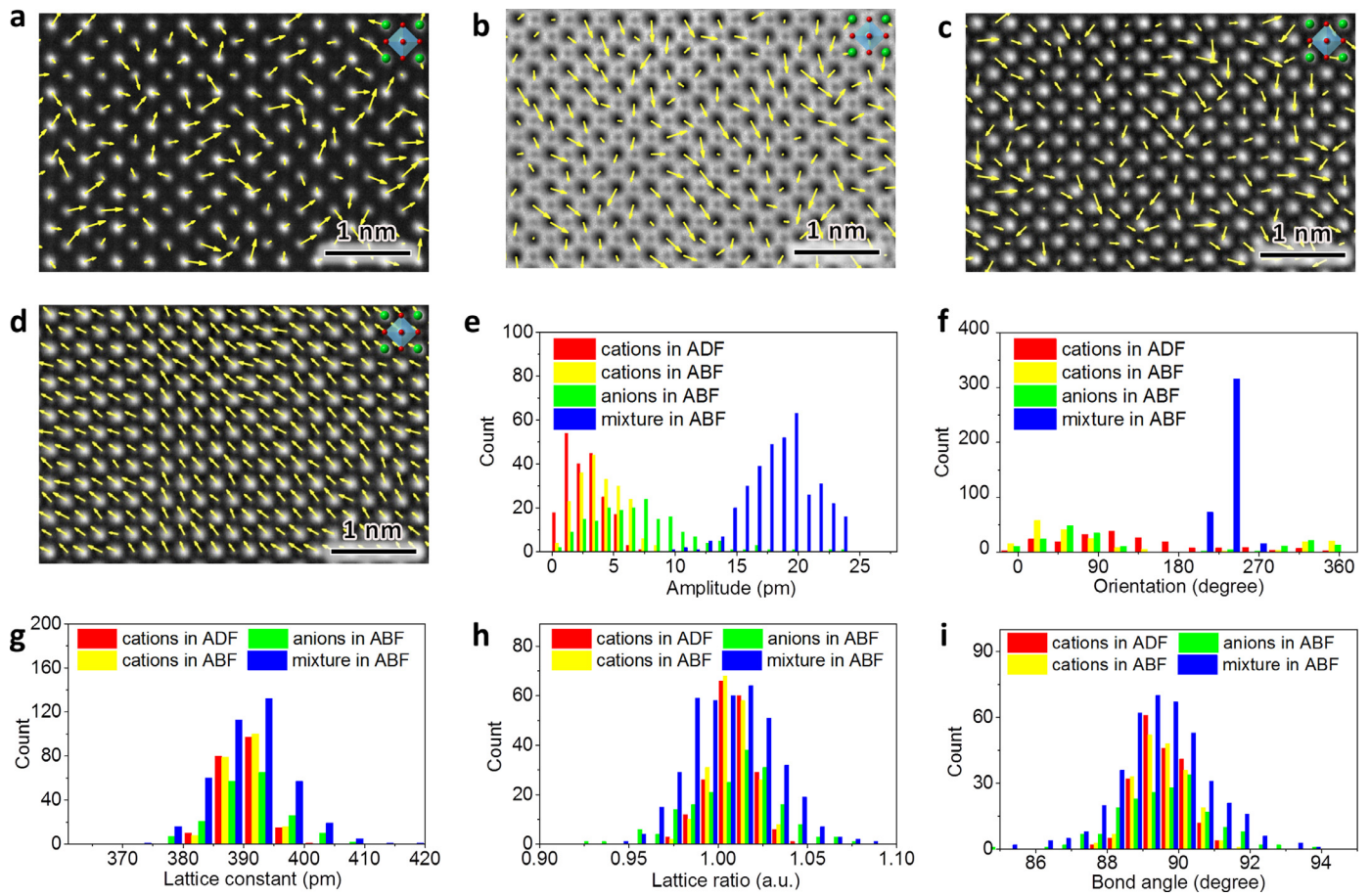
Fig. 3. Evaluation of specimen tilt and scan distortion from experimental ADF and ABF images. Maps of relative displacement vectors between (a) Sr and TiO columns in ADF, (b) Sr and TiO columns in ABF, (c) O and O columns in *I*-ABF, and (d) O and Sr/TiO columns in *I*-ABF images. For each A *vs* B configuration, the sign of vector is inverted for the *A*-type to maintain a constant direction in the mapping. Histogram distribution of (e) amplitude and (f) orientation of displacement vectors. Red: cation sub-lattice in ADF image. Yellow: cation sub-lattice in ABF image. Green: anion sub-lattice in *I*-ABF image. Blue: mixture sub-lattice *I*-ABF image. (g) Lattice constant, (h) Lattice ratio, and (i) Bond angle measurements. Red: cation sub-lattice in ADF image. Yellow: cation sub-lattice in ABF image. Green: anion sub-lattice in *I*-ABF image. Blue: mixture sub-lattice *I*-ABF image. (For interpretation of the references to color in this figure legend, the reader is referred to the web version of this article)

simulated aberration-free ADF and *I*-ABF images of STO with 25 nm thick, where we slightly mistilt the crystal along the [α β 1] direction from the [001] zone axis and the parameters of α and β are the mistilt angles in mrad (the reason we choose 25 nm as thickness is discussed below). No significant atom position shift is observed in the ADF images with α, $\beta \leq 10$ mrad, while severe displacement appears in the *I*-ABF images with mistilt α, $\beta \geq 6$ mrad. Although the respective cation and anion sub-lattices still remain square, their relative positions change dramatically. Once the mistilts of α, β are larger than 10 mrad, the position of anions becomes undistinguishable. To estimate the displacement vectors in these simulated images, the atom positions are fitted to 2D Gaussian function in the same manner. The amplitude of displacement between Sr and TiO columns in the simulated ADF images shown in Fig. 4(b) is calculated to be 3.3 pm with $\alpha = 10$ mrad, which is on the same level of the experimental scan distortion. Similar result is obtained from the simulated ABF image, suggesting no obvious dependence of artificial displacement in the cation sub-lattices at the collection angle of detectors. However, in ABF images, the displacement between cation and anion changes dramatically with specimen tilt. Only when the tilt α, $\beta \leq 4$ mrad, the displacement is small enough (≤ 2 pm). Once the misalignment increases to 6 mrad, the displacement reaches 11.9 pm that is much higher than that of scan distortion level. With $\alpha = \beta = 8$ mrad, the displacement is 42 pm which is equivalent to ~11% of lattice con-

stant. We note that, in the case without specimen tilt, the "background displacement" (systematic error: fitting noise) is only 0.027 pm for the simulated ADF and 0.048 pm for the simulated ABF, indicating the fitting noise is negligibly small compared to the mistilt effect. In Fig. 4(c), the displacement vectors in cation sub-lattice and mixture sub-lattice are orientated in different directions. With mistilt >2 mrad, the vectors calculated from mixture sub-lattice are orientated in the same direction, indicating the presence of significant artificial displacements.

The displacements between different atom species also rely on the defocus and thickness of specimen, because the probe propagation with the tilted crystal shows a dechanneling to the other atomic columns [34]. Fig. 5(a) is the simulated *I*-ABF images of STO with slightly off-axis [α β 1] with (α, β) = (8, 5) mrad. It clearly shows the displacements strongly depend on mistilt angles. Typical frames with various thickness and defocus are selected for 2D Gaussian fitting and the displacement vectors are estimated. The calculated amplitude and orientation of displacement are summarized in Fig. 5(b) and (c), respectively. By changing either thickness or defocus, the dependence behavior of amplitude is rather complicated. In our simulations, the relative displacements (>50 pm) for the mixture sub-lattice are maximized in the thickness range of 10–15 nm. The amplitude of displacements in ABF simulations also changes as a function of defocus. The dependence of orientation on thickness is not monotonous. When the thickness increases from
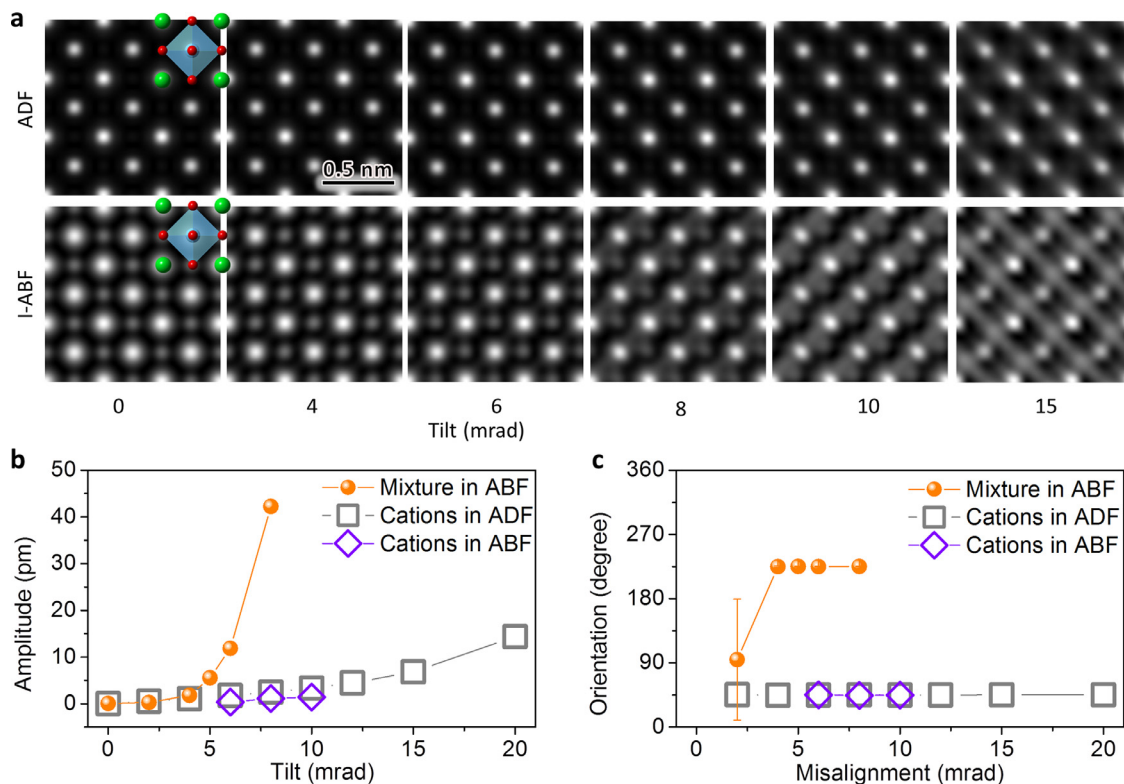
Fig. 4. Tilt dependence of displacement in STEM images of single crystal STO with thickness of 25 nm and defocus of 0 nm. (a) Simulated ADF and *I*-ABF images with various tilt: [α α 1], where α is the value of tilt angle. (b) Amplitude and (c) orientation of displacement vectors calculated from the simulated ADF and *I*-ABF images.
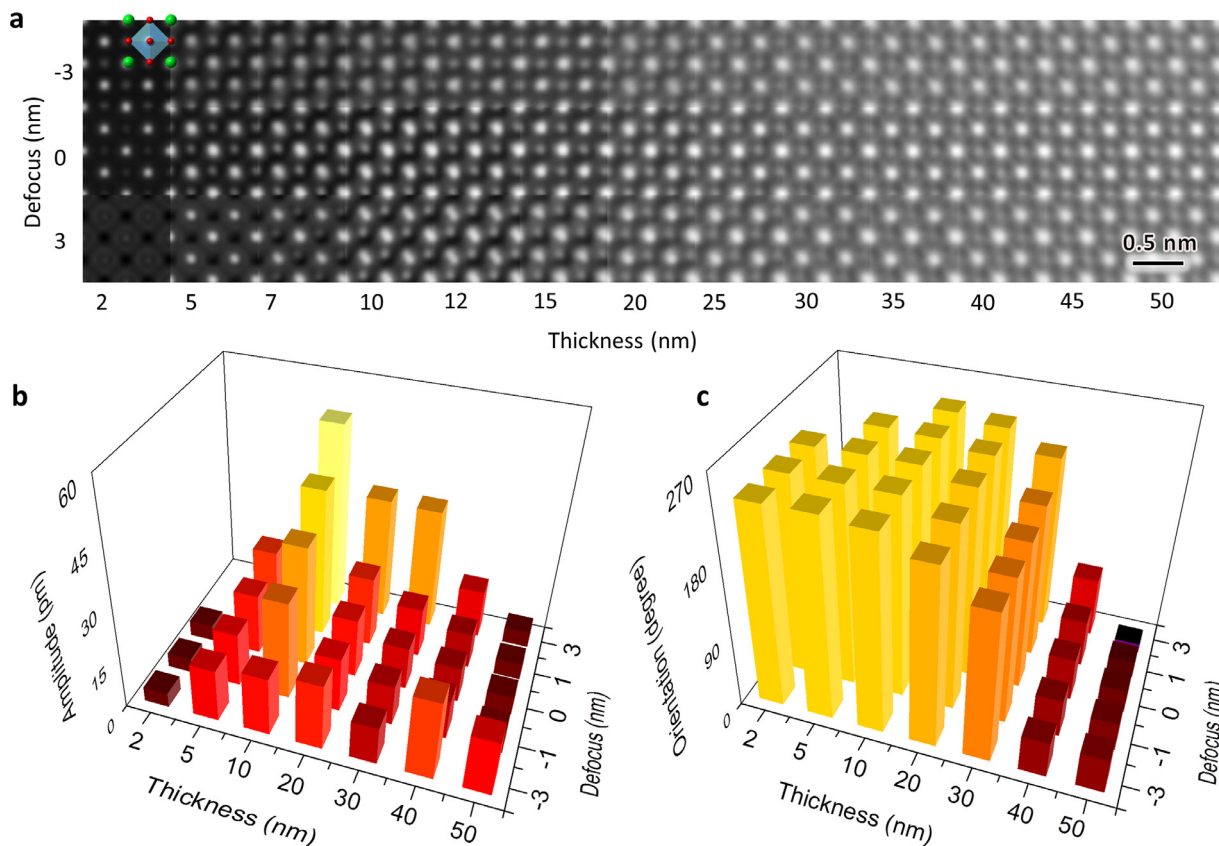
Fig. 5. Thickness and defocus dependence of displacement vectors in single crystal STO with zone axis [0.008 0.005 1]. (a) Simulated *I*-ABF images with different thickness and defocus. (b) Amplitude and (c) orientation of displacement vectors between O and Sr/TiO columns.
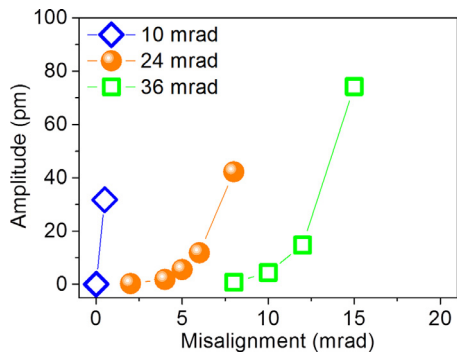
Fig. 6. Amplitude of displacement vectors between cation and oxygen columns in the simulated ABF images with thickness of 25 nm, defocus of 0 nm and various convergence and collection angles. Blue diamond: 10 mrad and [5,10] mrad for convergence semi-angle and collection angles. Orange ball: 24 mrad and [12,24] mrad. Green square: 36 mrad and [18,36]. (For interpretation of the references to color in this figure legend, the reader is referred to the web version of this article)

20 to 40 nm, the direction of displacement vectors becomes opposite. The defocus does not influence the orientation significantly.

Furthermore, for ADF images, increasing convergence angle has been proposed previously to reduce the impact of the tilt effect [27]. To investigate validity of larger illumination angles to the ABF imaging, we performed systematic image simulation with several convergence angles as well as collection angles (in order to match the 'hollow-cone illumination' conditions [11] to optimize the ABF contrast [8]). The displacements between cation and oxygen are plotted in Fig. 6. For the convergence angle of 10 mrad, the displacement in the mixture sub-lattice becomes over 30 pm only with 0.5 mrad mistilt. In this case, the artifact caused by the mistilt is an order of magnitude greater than that caused by the scan distortion. For the larger convergence angles, the displacement can be sufficiently reduced with a small mistilt. Therefore, it should be helpful to use a small illumination angle to detect the mistilt

during specimen alignment and a large illumination angle for ABF imaging to effectively reduce mistilt effects [55,57].

Since the measured displacement vectors in STEM images are affected by crystal tilt, specimen thickness, defocus, and convergence angle, we could find the practical parameters that can reproduce the artificial displacement in experiments with the aid of image simulations. Fig. 7(a) and (b) are simulated *I*-ABF image and corresponding vectors map along the zone axis of [α β 1] with $(\alpha, \beta) = (8, 5)$ mrad, thickness of 25 nm, defocus of 0.5 nm and the convergence semi-angle of 24 mrad. On the basis of the systematic investigations in simulated images, we find that the experimental data in Fig. 3(e) and (f) are in good agreement with the histograms of the amplitude and the orientation of displacement vectors in Fig. 7(c) and (d). Moreover, the simulated ABF intensity profiles with 25 nm thickness are matched with the experimental intensity profiles (Fig. 7(e) and (f)) very well. However, it should be noted that despite good agreement between experimental data and simulation, the experimental conditions are likely (more or less) different from simulation parameters due to the presence of coma, astigmatism, misalignments of aperture and detector, and therefore the simulated results can be considered as equivalent 'effective tilt' effects, which will be discussed later. Nevertheless, the simulation can help us to effectively determine the specimen tilt and thus correct the artificial displacements.

4. Discussion

To reveal why the atom positions in ABF image is sensitive to the specimen tilt, we calculated the probe intensity propagation in the STO in Fig. 8, where the electron beam is focused on the entrance surface of the Sr column, center of left Sr and right O, O column, and center of left O and right Sr. Without tilt, for the electron beam on Sr in Fig. 8(a), only a few electrons go to the ABF detector (shadowed regions), explaining the dark contrast for Sr atom position in the ABF image (or bright contrast in *I*-ABF image) [8]. For the contrast of O atom position in the ABF image, the
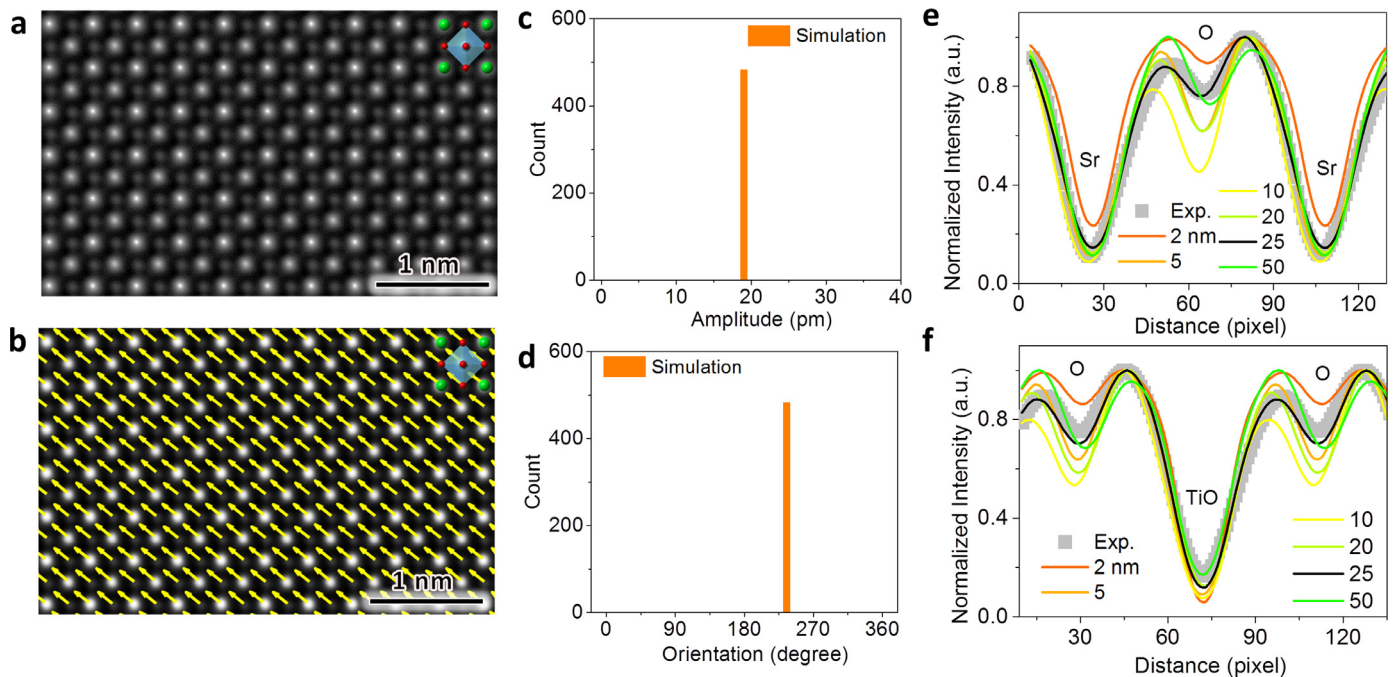
Fig. 7. Simulation of STO with viewing direction of [0.008 0.005 1], thickness of 25 nm and defocus of 0.5 nm. (a) Simulated *I*-ABF image. (b) Corresponding map of displacement vectors between O and Sr/TiO columns in the simulated *I*-ABF image. The sign of displacement vector is inverted for the first O to maintain a constant direction in the mapping. Histogram distribution of (c) amplitude and (d) orientation of displacement vectors. (e, f) Thickness-dependent intensity profiles showing 25 nm (black curves) is close to the experimental data (grey squares). (For interpretation of the references to color in this figure legend, the reader is referred to the web version of this article)
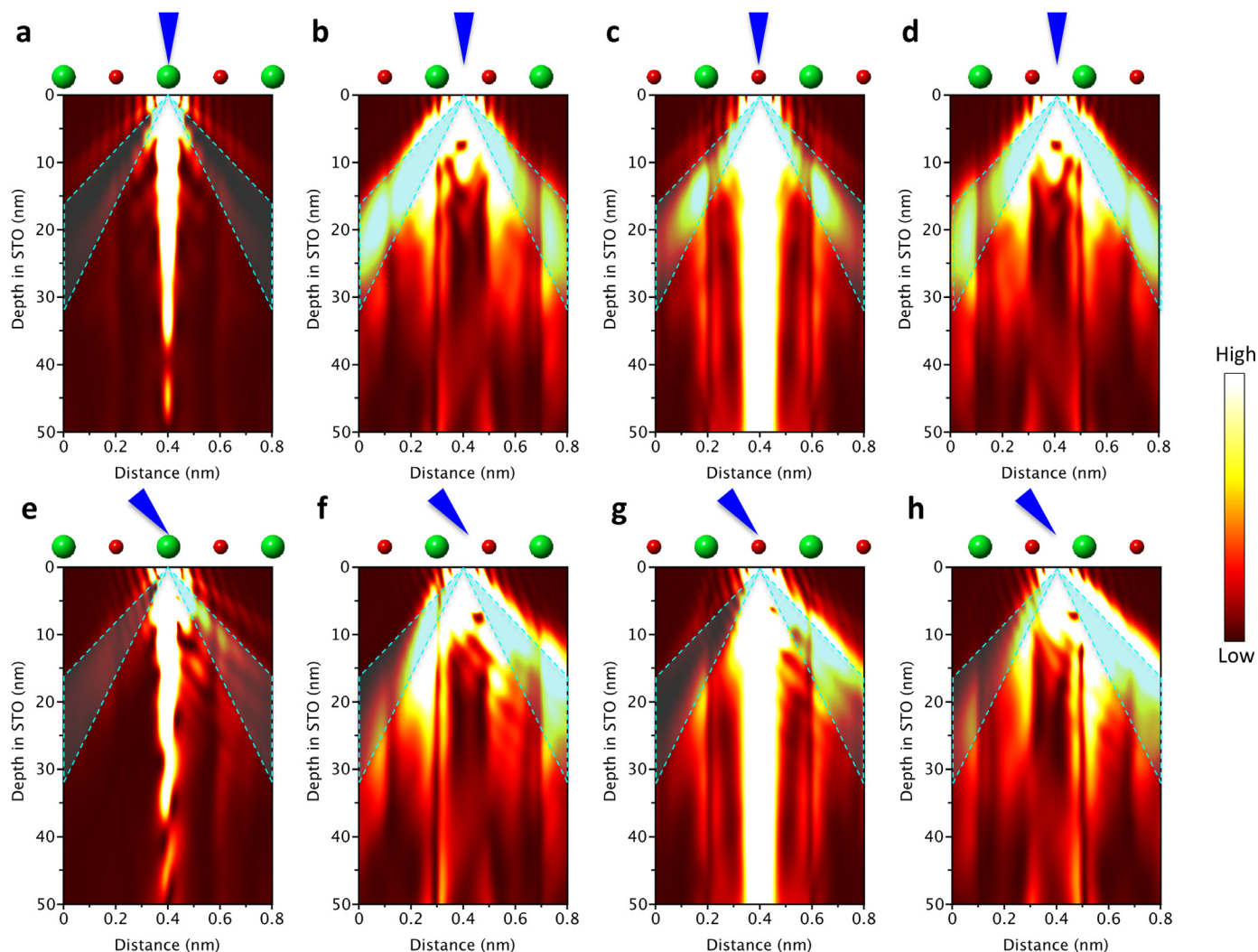
Fig. 8. Calculated beam propagation in the STO with convergence angle of 24 mrad. The electron beam is focused on (a) Sr column, (b) the center of left Sr and right O, (c) O column, and (d) the center of left O and right Sr. Zone axis is [0 0 1] with no specimen tilt. The green atom indicates the Sr atom position and red atom indicates the O position. The shadowed regions highlight the ABF detector collection range. With specimen tilt, the electron beam is focused on (e) Sr column, (f) the center of left Sr and right O, (g) O column, and (h) the center of left O and right Sr. The zone axis is [0.008 0 1]. (For interpretation of the references to color in this figure legend, the reader is referred to the web version of this article)

interpretation is similar except the amount of electrons collected by the ABF detector is larger [8]. For the electron beam on the gap between the atom columns (Fig. 8(b) and (d)), the electrons are scattered into two branches in the projection (conical in 3D space), most of which are collected by the ABF detector as shown in Fig. 8(b) and (d). With the specimen tilt in Fig. 8(e) ($\alpha = 8$ mrad), the electron probe propagation along the Sr column periodically oscillates through the thickness. In this case, the amount of electrons going to the ABF detector increases due to the enhanced de-channeling effect, corresponding to the weaker signal for the Sr atom position. For the tilted electron beam on the gap (or tilted specimen), these two braches of scattered electrons rotate anti-clockwise. In other words, part of electrons in the left branch are scattered into the lower angle (smaller than 12 mrad) while part of electrons in the right branch are scattered to higher angle (larger than 24 mard). These scattered electrons are no longer collected by the ABF defector, leading to reduction of signal for the gap in the ABF image. As a result, the contrast between the atom column and gap becomes reduced or even inverted. This can explain that the tilt induces the atom position shift. Due to the lighter mass for the O, the tilt induced relative contrast change between atom column

and gap is more significant in Fig. 8, and thus the atom position shift is more pronounced.

In the case of specimen tilt, during image recording we usually deliberately introduce coma and astigmatism to partly compensate the tilt effect thus to get better visual appearance of the atom shape. Therefore, the specimen tilt can not only directly affect the positions of atom columns in STEM images but also indirectly influence the contrast via introduction of aberration. To evaluate the effects of aberration, the simulated ABF images with different A_1, A_2, B_2 and C_3 are shown in Fig. 9. When the A_2 or B_2 is smaller than 50 nm, the displacement is less than 5 pm that is at the level of experimental error such as scan distortion. Note that, in our experiments, we use the automated software to set up the values of A_2 and B_2 less than 20 nm at amorphous regions [58]. In this regard, the net effects of aberration are negligible on the quantitative position analysis. Consequently, most of the quantitative discussion below is based on the direct tilt effect in the simulation, but these conclusions should be qualitatively applicable to experimental data.

To quantitatively discuss the crystal tilt effect on precise position measurement, we define an 'effective sub-lattice', within which calculations between any atom columns remain effective. In
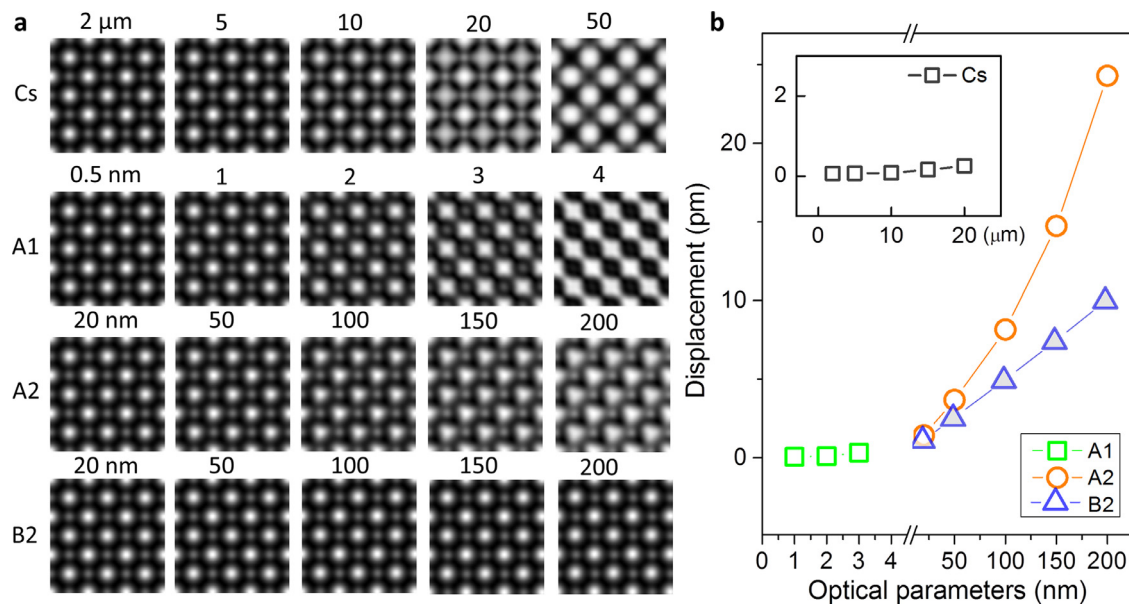
Fig. 9. Aberration dependence of displacement in single crystal STO with zone axis [0 0 1]. (a) Simulated *I*-ABF images. (b) Amplitude of displacements in the *I*-ABF images with aberration.

the case of perfect zone axis ($\alpha = 0$), the entire lattice is an effective sub-lattice. With small tilt $\alpha \leq 4$ mrad for ~ 25 nm thick STO, since all types of displacements are small enough (<2 pm), the entire lattice can still be treated as an effective sub-lattice. Once the mistilt is $\alpha > 5$ mrad, the displacement between O and cations columns is ~ 11.9 pm for $\alpha = 6$ mrad that is well above the level of scan distortion. Therefore, the anion and cation columns in STO are no longer in the same effective sub-lattice, but the Sr and TiO columns can be still considered within the same effective sub-lattice if the tilt is ≤ 10 mrad. For large crystal mistilt > 15 mrad, the Sr and TiO columns are not within the same effective sub-lattice any more. However, respective Sr, TiO and O columns are intrinsically in the same effective sub-lattice regardless of tilt as they have the same shift behavior on tilt, indicating unlike scan distortion the specimen tilt will not affect the measurement of lattice constant, lattice ratio and angle between lattice vectors, which is very useful to distinguish the specimen tilt during image analysis [13,14].

5. Conclusions

The effects of specimen tilt on the picometer-scale measurement of atom positions for ABF-STEM images are studied by combining the experiments and simulations. By using the relative distance measurement method, we are able to effectively distinguish the effects of crystal tilt from scan distortion. Thus, it is possible to quantitatively evaluate the specimen tilt effects on the atom position analysis. The main conclusions are given below:

(1) For ABF imaging, small tilt on the order of ~ 6 mrad can cause an artificial displacement 11.9 pm between anion and cation positions under typical experimental conditions for cubic STO. This value is 3 or 4 times larger than the scan distortion (3.2 pm), suggesting the specimen tilt is critical for picometre-scale measurement of ABF images.

(2) The tilt-induced artifact relies on the tilt angle, thickness of specimen, defocus and convergence angle. During specimen alignment, changing defocus and using small aperture is helpful to detect and correct the specimen tilt. However, larger aperture is preferable for imaging to minimize the artifact.

(3) Although the residual aberrations can also influence on the atom position analysis, the effects of aberration is difficult to separate from the net mistilt in the experimental images. Generally, small A_2 and B_2 (<50 nm) would not cause significant artifact on displacements measurement.

(4) The effective sub-lattices can help us to evaluate the effects of tilt. The effects of small mistilt in ADF images is negligible because the cation columns such as Sr and TiO have similar dechannelling behavior (while the light atoms are invisible). The pure tilt effect has no influence on the lattice constant measurement because the crystallographically same atom columns have the same atom shift.

(5) The tilt redistributes crystal-scattered electrons and thus changes the relative contrast between the atom columns and gap, accounting for the atom position shift and artificial displacements.

(6) The relative displacement measurement method that can effectively separate the tilt effect from the scan distortion can be used to quantitatively evaluate the tilt effect and also distinguish the specimen tilt during data analysis. Multislice simulation of STEM images can be used to quantitatively estimate tilt effects in the experiments, and thus help us to extract the true atomic configurations.

These findings provide useful insights into quantitative atom position analysis based on STEM images.

for Thousand Young Talents of China and '2011 Program' Peking-Tsinghua-IOP Collaborative Innovation Centre for Quantum Matter.

References

[1] S. Bals, S. Van Aert, G. Van Tendeloo, D. Avila-Brande, Statistical estimation of atomic positions from exit wave reconstruction with a precision in the picometer range, Phys. Rev. Lett. 96 (2006) 096106.

[2] C.-L. Jia, V. Nagarajan, J.-Q. He, L. Houben, T. Zhao, R. Ramesh, K. Urban, R. Waser, Unit-cell scale mapping of ferroelectricity and tetragonality in epitaxial ultrathin ferroelectric films, Nature Mater. 6 (2007) 64–69.

[3] C.T. Nelson, B. Winchester, Y. Zhang, S.-J. Kim, A. Melville, C. Adamo, C.M. Folkman, S.-H. Baek, C.-B. Eom, D.G. Schlom, L.-Q. Chen, X. Pan, Spontaneous vortex nanodomain arrays at ferroelectric heterointerfaces, Nano Lett. 11 (2011) 828–834.

[4] C.-L. Jia, S.-B. Mi, K. Urban, I. Vrejoiu, M. Alexe, D. Hesse, Atomic-scale study of electric dipoles near charged and uncharged domain walls in ferroelectric films, Nature Mater. 7 (2008) 57–61.

[5] A.B. Yankovich, B. Berkels, W. Dahmen, P. Binev, S.I. Sanchez, S.A. Bradley, A. Li, I. Szlufarska, P.M. Voyles, Picometre-precision analysis of scanning transmission electron microscopy images of platinum nanocatalysts, Nature Commun. 5 (2014) 4155.

[6] A.V. Crewe, J. Wall, J. Langmore, Visibility of single atoms, Science 168 (1970) 1338-&.

[7] S.J. Pennycook, Z-contrast STEM for materials science, Ultramicroscopy 30 (1989) 58–69.

[8] S.D. Findlay, N. Shibata, H. Sawada, E. Okunishi, Y. Kondo, Y. Ikuhara, Dynamics of annular bright field imaging in scanning transmission electron microscopy, Ultramicroscopy 110 (2010) 903–923.

[9] E. Okunishi, I. Ishikawa, H. Sawada, F. Hosokawa, M. Hori, Y. Kondo, Visualization of light elements at ultrahigh resolution by STEM annular bright field microscopy, Microsc. Microanal. 15 (2009) 164–165.

[10] S.D. Findlay, T. Saito, N. Shibata, Y. Sato, J. Matsuda, K. Asano, E. Akiba, T. Hirayama, Y. Ikuhara, Direct imaging of hydrogen within a crystalline environment, Appl. Phys. Express 3 (2010) 116603.

[11] R. Ishikawa, E. Okunishi, H. Sawada, Y. Kondo, F. Hosokawa, E. Abe, Direct imaging of hydrogen-atom columns in a crystal by annular bright-field electron microscopy, Nature Mater. 10 (2011) 278–281.

[12] R. Huang, Y.H. Ikuhara, T. Mizoguchi, S.D. Findlay, A. Kuwabara, C.A.J. Fisher, H. Moriwake, H. Oki, T. Hirayama, Y. Ikuhara, Oxygen-vacancy ordering at surfaces of lithium manganese(III,IV) oxide spinel nanoparticles, Angewandte Chemie-Int. Ed. 50 (2011) 3053–3057.

[13] P. Gao, H.-J. Liu, Y.-L. Huang, Y.-H. Chu, R. Ishikawa, B. Feng, Y. Jiang, N. Shibata, E.-G. Wang, Y. Ikuhara, Atomic mechanism of polarization-controlled surface reconstruction in ferroelectric thin films, Nature Commun. 7 (2016) 11318.

[14] P. Gao, Z. Zhang, M. Li, R. Ishikawa, B. Feng, H.-J. Liu, Y.-L. Huang, N. Shibata, X. Ma, S. Chen, J. Zhang, K. Liu, E.-G. Wang, D. Yu, L. Liao, Y.-H. Chu, Y. Ikuhara, Possible absence of critical thickness and size effect in ultrathin perovskite ferroelectric films, Nature Commun. 8 (2017) 15549.

[15] Y.-M. Kim, S.J. Pennycook, A.Y. Borisevich, Quantitative comparison of bright field and annular bright field imaging modes for characterization of oxygen octahedral tilts, Ultramicroscopy 181 (2017) 1–7.

[16] D. Kan, R. Aso, H. Kurata, Y. Shimakawa, Unit-cell thick BaTiO$_3$ blocks octahedral tilt propagation across oxide heterointerface, J. Appl. Phys. 115 (2014) 184304.

[17] K.Z. Baba-Kishi, A.M. Glazer, Local structure of Pb(Zr$_{0.53}$Ti$_{0.47}$)O$_3$, J. Appl. Crystallogr. 47 (2014) 1688–1698.

[18] R. Aso, D. Kan, Y. Shimakawa, H. Kurata, Control of structural distortions in transition-metal oxide films through oxygen displacement at the heterointerface, Adv. Funct. Mater. 24 (2014) 5177–5184.

[19] R. Aso, D. Kan, Y. Shimakawa, H. Kurata, Octahedral tilt propagation controlled by A-Site cation size at perovskite oxide heterointerfaces, Crystal Growth Des. 14 (2014) 2128–2132.

[20] R. Aso, D. Kan, Y. Shimakawa, H. Kurata, Atomic level observation of octahedral distortions at the perovskite oxide heterointerface, Sci. Rep. 3 (2013) 2214.

[21] J.-M. Zuo, A.B. Shah, H. Kim, Y. Meng, W. Gao, J.-L. Rouviere, Lattice and strain analysis of atomic resolution Z-contrast images based on template matching, Ultramicroscopy 136 (2014) 50–60.

[22] X. Sang, J.M. LeBeau, Revolving scanning transmission electron microscopy: correcting sample drift distortion without prior knowledge, Ultramicroscopy 138 (2014) 28–35.

[23] L. Jones, P.D. Nellist, Testing the accuracy of the two-dimensional object model in HAADF STEM, Micron 63 (2014) 47–51.

[24] C. Ophus, J. Ciston, C.T. Nelson, Correcting nonlinear drift distortion of scanning probe and scanning transmission electron microscopies from image pairs with orthogonal scan directions, Ultramicroscopy 162 (2016) 1–9.

[25] D. Van Dyck, R.M.J. Bokel, H.W. Zandbergen, Does crystal tilt enhance the electron interaction? Microsc. Microanal. 4 (1998) 428–434.

[26] S.E. Maccagnano-Zacher, K.A. Mkhoyan, E.J. Kirkland, J. Silcox, Effects of tilt on high-resolution ADF-STEM imaging, Ultramicroscopy 108 (2008) 718–726.

[27] Y.-G. So, K. Kimoto, Effect of specimen misalignment on local structure analysis using annular dark-field imaging, J. Electron Microsc. 61 (2012) 207–215.

[28] P. Wang, A.L. Bleloch, U. Falke, P.J. Goodhew, Geometric aspects of lattice contrast visibility in nanocrystalline materials using HAADF STEM, Ultramicroscopy 106 (2006) 277–283.

[29] X. Wu, M.D. Robertson, M. Kawasaki, J.M. Baribeau, Effects of small specimen tilt and probe convergence angle on ADF-STEM image contrast of Si$_{0.8}$Ge$_{0.2}$ epitaxial strained layers on (100) Si, Ultramicroscopy 114 (2012) 46–55.

[30] T. Yamazaki, M. Kawasaki, K. Watanabe, I. Hashimoto, M. Shiojiri, Effect of small crystal tilt on atomic-resolution high-angle annular dark field STEM imaging, Ultramicroscopy 92 (2002) 181–189.

[31] Z. Yu, D.A. Muller, J. Silcox, Effects of specimen tilt in ADF-STEM imaging of a-Si/c-Si interfaces, Ultramicroscopy 108 (2008) 494–501.

[32] Z. Wang, J. Tao, L. Yu, H. Guo, L. Chen, M.-G. Han, L. Wu, H. Xin, K. Kisslinger, E.W. Plummer, Anomalously deep polarization in SrTiO$_3$ (001) interfaced with an epitaxial ultrathin manganite film, Phys. Rev. B 94 (2016) 155307.

[33] J. Cui, Y. Yao, Y.G. Wang, X. Shen, R.C. Yu, The origin of atomic displacements in HAADF images of the tilted specimen, Ultramicroscopy 182 (2017) 156–162.

[34] R.F. Loane, E.J. Kirkland, J. Silcox, Visibility of single heavy-atoms on thin crystalline silicon in simulated annular dark-field STEM images, Acta Crystallogr. Section A 44 (1988) 912–927.

[35] P. Gao, A. Kumamoto, R. Ishikawa, N.R. Lugg, N. Shibata, Y. Ikuhara, Misalignment induced artifacts in quantitative annular bright-field imaging, Microsc Microanal. 22 (2016) 888–889.

[36] D. Zhou, K. Mueller-Caspary, W. Sigle, F.F. Krause, A. Rosenauer, P. van Aken, Sample tilt effects on atom column position determination in ABF-STEM imaging, Ultramicroscopy 160 (2016) 110–117.

[37] Y. Liu, Y.L. Zhu, Y.L. Tang, X.L. Ma, An effect of crystal tilt on the determination of ions displacements in perovskite oxides under BF/HAADF-STEM imaging mode, J. Mater. Res. 32 (2017) 947–956.

[38] H.G. Brown, R. Ishikawa, G. Sanchez-Santolino, N.R. Lugg, Y. Ikuhara, L.J. Allen, N. Shibata, A new method to detect and correct sample tilt in scanning transmission electron microscopy bright-field imaging, Ultramicroscopy 173 (2017) 76–83.

[39] C.-L. Jia, K.W. Urban, M. Alexe, D. Hesse, I. Vrejoiu, Direct observation of continuous electric dipole rotation in flux-closure domains in ferroelectric Pb(Zr,Ti)O$_3$, Science 331 (2011) 1420–1423.

[40] M.F. Chisholm, W. Luo, M.P. Oxley, S.T. Pantelides, H.N. Lee, Atomic-scale compensation phenomena at polar interfaces, Phys. Rev. Lett. 105 (2010) 197602.

[41] A. Lubk, M.D. Rossell, J. Seidel, Q. He, S.Y. Yang, Y.H. Chu, R. Ramesh, M.J. Hytch, E. Snoeck, Evidence of sharp and diffuse domain walls in BiFeO$_3$ by means of unit-cell-wise strain and polarization maps obtained with high resolution scanning transmission electron microscopy, Phys. Rev. Lett. 109 (2012) 047601.

[42] Y.-M. Kim, J. He, M.D. Biegalski, H. Ambaye, V. Lauter, H.M. Christen, S.T. Pantelides, S.J. Pennycook, S.V. Kalinin, A.Y. Borisevich, Probing oxygen vacancy concentration and homogeneity in solid-oxide fuel-cell cathode materials on the subunit-cell level, Nature Mater. 11 (2012) 888–894.

[43] A. Borisevich, O.S. Ovchinnikov, H.J. Chang, M.P. Oxley, P. Yu, J. Seidel, E.A. Eliseev, A.N. Morozovska, R. Ramesh, S.J. Pennycook, Mapping octahedral tilts and polarization across a domain wall in BiFeO$_3$ from Z-Contrast scanning transmission electron microscopy image atomic column shape analysis, Acs. Nano 4 (2010) 6071–6079.

[44] A.Y. Borisevich, H.J. Chang, M. Huijben, M.P. Oxley, S. Okamoto, M.K. Niranjan, J.D. Burton, E.Y. Tsymbal, Y.H. Chu, P. Yu, R. Ramesh, S.V. Kalinin, S.J. Pennycook, Suppression of octahedral tilts and associated changes in electronic properties at epitaxial oxide heterostructure interfaces, Phys. Rev. Lett. 105 (2010) 087204.

[45] C.T. Nelson, P. Gao, J.R. Jokisaari, C. Heikes, C. Adamo, A. Melville, S.-H. Baek, C.M. Folkman, B. Winchester, Y. Gu, Y. Liu, K. Zhang, E. Wang, J. Li, L.-Q. Chen, C.-B. Eom, D.G. Schlom, X. Pan, Domain dynamics during ferroelectric switching, Science 334 (2011) 968–971.

[46] P. Gao, J. Britson, J.R. Jokisaari, C.T. Nelson, S.-H. Baek, Y. Wang, C.-B. Eom, L.-Q. Chen, X. Pan, Atomic-scale mechanisms of ferroelastic domain-wall-mediated ferroelectric switching, Nature Commun. 4 (2013) 2791.

[47] P. Gao, J. Britson, C.T. Nelson, J.R. Jokisaari, C. Duan, M. Trassin, S.-H. Baek, H. Guo, L. Li, Y. Wang, Y.-H. Chu, A.M. Minor, C.-B. Eom, R. Ramesh, L.-Q. Chen, X. Pan, Ferroelastic domain switching dynamics under electrical and mechanical excitations, Nature Commun. 5 (2014) 3801.

[48] P. Gao, C.T. Nelson, J.R. Jokisaari, S.-H. Baek, C.W. Bark, Y. Zhang, E. Wang, D.G. Schlom, C.-B. Eom, X. Pan, Revealing the role of defects in ferroelectric switching with atomic resolution, Nature Commun. 2 (2011) 591.

[49] P. Gao, C.T. Nelson, J.R. Jokisaari, Y. Zhang, S.-H. Baek, C.W. Bark, E. Wang, Y. Liu, J. Li, C.-B. Eom, X. Pan, Direct observations of retention failure in ferroelectric memories, Adv. Mater. 24 (2012) 1106–1110.

[50] S. Van Aert, S. Turner, R. Delville, D. Schryvers, G. Van Tendeloo, E.K.H. Salje, Direct observation of ferrielectricity at ferroelastic domain boundaries in CaTiO$_3$ by electron microscopy, Adv. Mater. 24 (2012) 523-+.

[51] L. Li, P. Gao, C.T. Nelson, J.R. Jokisaari, Y. Zhang, S.-J. Kim, A. Melville, C. Adamo, D.G. Schlom, X. Pan, Atomic scale structure changes induced by charged domain walls in ferroelectric materials, Nano Lett. 13 (2013) 5218–5223.

[52] Y.L. Tang, Y.L. Zhu, X.L. Ma, A.Y. Borisevich, A.N. Morozovska, E.A. Eliseev, W.Y. Wang, Y.J. Wang, Y.B. Xu, Z.D. Zhang, Observation of a periodic array of flux-closure quadrants in strained ferroelectric PbTiO$_3$ films, Science 348 (2015) 547–551.

[53] Y.L. Tang, Y.L. Zhu, Y.J. Wang, W.Y. Wang, Y.B. Xu, W.J. Ren, Z.D. Zhang, X.L. Ma, Atomic-scale mapping of dipole frustration at 90° charged domain walls in ferroelectric PbTiO₃ films, Sci. Rep. 4 (2014) 4115.

[54] Y.A. Abramov, V.G. Tsirelson, V.E. Zavodnik, S.A. Ivanov, I.D. Brown, The chemical bond and atomic displacements in SrTiO₃ from x-ray diffraction analysis, Acta Crystallogr. Section B-Struct. Sci. 51 (1995) 942–951.

[55] R. Ishikawa, A.R. Lupini, S.D. Findlay, S.J. Pennycook, Quantitative annular dark field electron microscopy using single electron signals, Microsc. Microanal. 20 (2014) 99–110.

[56] W. Zhong, R.D. Kingsmith, D. Vanderbilt, Giant LO-TO splitting sin perovskite ferroelectrics, Phys. Rev. Lett. 72 (1994) 3618–3621.

[57] R. Ishikawa, S.J. Pennycook, A.R. Lupini, S.D. Findlay, N. Shibata, Y. Ikuhara, Single atom visibility in STEM optical depth sectioning, Appl. Phys. Lett. 109 (2016) 163102.

[58] F. Hosokawa, H. Sawada, Y. Kondo, K. Takayanagi, K. Suenaga, Development of Cs and Cc correctors for transmission electron microscopy, Microscopy 62 (2013) 23–41.